

Wake-Induced Oscillatory Paths of Bodies Freely Rising or Falling in Fluids

Patricia Ern, Frédéric Risso, David Fabre,
and Jacques Magnaudet

Institut de Mécanique des Fluides de Toulouse, Université de Toulouse and CNRS,
31400 Toulouse, France; email: Jacques.Magnaudet@imft.fr

Annu. Rev. Fluid Mech. 2012. 44:97–121

First published online as a Review in Advance on
September 9, 2011

The *Annual Review of Fluid Mechanics* is online at
fluid.annualreviews.org

This article's doi:
10.1146/annurev-fluid-120710-101250

Copyright © 2012 by Annual Reviews.
All rights reserved

0066-4189/12/0115-0097\$20.00

Keywords

falling body, rising bubble, wake instability, path instability, lift force,
added mass

Abstract

Leaves falling in air and bubbles rising in water provide daily examples of nonstraight paths associated with the buoyancy-driven motion of a body in a fluid. Such paths are relevant to a large variety of applicative fields such as mechanical engineering, aerodynamics, meteorology, and the biomechanics of plants and insect flight. Although the problem has attracted attention for ages, it is only recently that the tremendous progress in the development of experimental and computational techniques and the emergence of new theoretical concepts have led to a better understanding of the underlying physical mechanisms. This review attempts to bring together the main recent experimental, computational, and theoretical advances obtained on this fascinating subject. To this end it describes the first steps of the transition in the wake of a fixed body and its connection with the onset and development of the path instability of moving bodies. Then it analyzes the kinematics and dynamics of various types of bodies along typical nonstraight paths and how the corresponding information can be used to build low-dimensional predictive models.

PIV: particle image
velocimetry
DNS: direct
numerical simulation

1. INTRODUCTION

Bodies with widely different sizes, weights, and shapes may describe various periodic or chaotic nonstraight paths when rising or falling under the effect of gravity in a fluid otherwise at rest. Understanding the origin and nature of these nonstraight paths has continuously been a focus of concern arising from many domains, such as meteorology [hailstone growth (Kry & List 1974)], sedimentology [suspension time of sedimenting particles and its consequences on bed erodibility and roughness (Stringham et al. 1969)], and the mechanics of insect flight [aerodynamic forces experienced by flying insects, in particular in hovering flight (see Wang 2005)]. In ecology, plume and winged seeds spreading out from trees also are capable of various aerial movements (Augsburger 1986, Burrows 1975, Lentink et al. 2009), resulting in a differential dispersal capacity, considered as key to the coexistence of plants. Besides these natural situations, buoyancy-driven body paths are closely related to several fundamental questions in aerodynamics and marine engineering, especially to the understanding of autorotation (Lugt 1983) and of vortex-induced vibrations on loosely tethered bodies (Williamson & Govardhan 2004). They are also widely encountered in engineering processes involving dispersed two-phase flows. In these, path oscillations are found to be robust to perturbations affecting the surrounding fluid, such as turbulence (Ford & Loth 1998) or interactions with neighboring bodies (Riboux et al. 2010), making results obtained for isolated bodies relevant to multiphase flows (Magnaudet & Eames 2000). Since the early days of fluid mechanics, some of the greatest names in physics, especially Leonardo (see Prosperetti et al. 2003, Prosperetti 2004), Newton (1687) (see also Viets & Lee 1971), Kirchhoff (1869), Maxwell (1853), and Eiffel (1912), have contributed to identify the distinctive features of buoyancy-driven body paths, such as the existence of periodic and irregular motions, the influence of the body shape, the drag modification due to nonstraight paths, and the connection with the movements induced in the surrounding fluid. They also partly set the theoretical basis on which further studies were built. The problem was tirelessly investigated during the twentieth century. Nevertheless, it was only recently that the three-pronged approach of sophisticated optical techniques [high-speed imaging and particle image velocimetry (PIV)], direct numerical simulation (DNS), and to some extent, hydrodynamic instability theory led to decisive improvements in our understanding of this class of phenomena.

The aim of this review is to provide an overview of the current knowledge that has resulted from the various streams of investigation and of the new issues that arose from them. We restrict our attention to the case of homogeneous bodies with simple geometries, essentially nominally two-dimensional bodies such as plates and circular cylinders whose span is much larger than any other characteristic dimension and axisymmetric bodies such as spheroids and disks of various thicknesses. For such bodies falling or rising under the effect of buoyancy in a Newtonian fluid at rest at infinity, the problem is governed by three control parameters, namely the body-to-fluid density ratio $\bar{\rho}$; the Archimedes number Ar , which is basically a Reynolds number built on some characteristic length scale d of the body and on the gravitational velocity scale $V_g = (1 - \bar{\rho})g d)^{1/2}$ (where g denotes gravity); and a geometrical parameter χ characterizing the geometric anisotropy of the body. Although the body velocity is an outcome of the experiment, it is also useful to introduce the Reynolds number Re based on the mean vertical velocity of the body U_m , as the phenomena to be discussed below basically take place at moderate values of this parameter, typically $10^2 \leq Re \leq 10^4$, which clearly corresponds to flow regimes in which the wake past the body plays a dominant role. The various situations investigated in the literature are mapped out in the parameter space $(\bar{\rho}, \chi, Re)$ in **Figure 1**. This figure reveals that an even coverage of the parametrical space is clearly missing, with the conditions investigated to date being quite different. This is partly why a division based on the geometrical type of body considered, although undesirable in principle, remains the most appropriate and is used throughout this review.

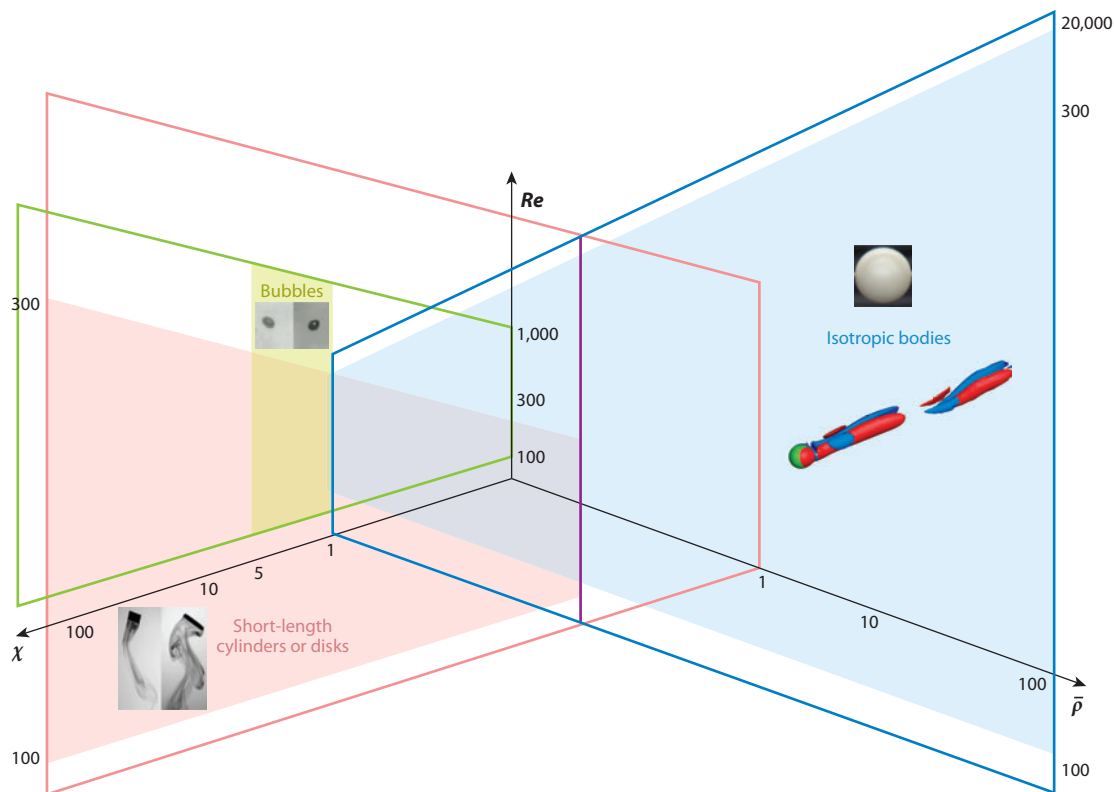


Figure 1

Mapping of the situations investigated to date in the three-dimensional space of control parameters $(\bar{\rho}, \chi, Re)$.

The interplay between the body degrees of freedom and the wake dynamics is at the heart of this article, with the fundamental role of vorticity production at the body surface as the backdrop. We discuss the various aspects of wake-induced loads associated with wake instabilities and their consequences on the body path, as well as the reverse effect of the body degrees of freedom on the wake dynamics. Section 2 summarizes the various possible causes of path oscillations. Section 3 provides an overview of the first stages of the transition in the wake of a fixed body, a necessary step to better understand the occurrence and the first stages of oscillatory motions of freely moving bodies, as discussed in Section 4. The relationship between the kinematics and dynamics of the body, and their relationship with the wake dynamics, is the subject of Section 5. A significant part of this section deals with recent attempts at building low-dimensional models of forces and torques acting on the body, capable of reproducing the observed paths. Section 6 summarizes the main points raised in the review and provides some suggestions for future research.

2. CAUSES OF PATH OSCILLATIONS

The dynamics of a rigid body immersed in a Newtonian fluid at rest at infinity results from the coupling between the body motion and the surrounding flow field, which is a solution of the Navier-Stokes equations satisfying initial and boundary conditions both at the body surface and far from it. The minimal description of the fluid flow that can be considered reduces to the

loads—forces and torques—it exerts on the body. These hydrodynamical efforts include added inertia (also often referred to as added mass) contributions resulting from the instantaneous reaction of the fluid to a body displacement (translation and/or rotation), which are determined entirely by the body shape and do not depend on the vorticity generated at its surface, nor on that which may eventually exist in the core of the fluid. This property of added inertia effects makes it possible to separate them unambiguously from contributions to the force and torque induced by the presence of vorticity around the body (Howe 1995). Therefore, the classical Kelvin-Kirchhoff equations expressing linear and angular momentum conservation for the coupled fluid/body system when the flow around the body is assumed irrotational may actually be extended to any incompressible flow containing vorticity. For a rigid body with three mutually orthogonal symmetry planes and moving in a fluid at rest at infinity, these extended Kelvin-Kirchhoff equations expressed in a reference frame having its origin fixed with respect to the laboratory but axes rotating with the body read

$$(\bar{\rho}\mathbb{I} + \mathbb{A}) \cdot \frac{d\mathbf{U}}{dt} + \boldsymbol{\Omega} \times [(\bar{\rho}\mathbb{I} + \mathbb{A}) \cdot \mathbf{U}] = \mathbf{F}_\omega + (\bar{\rho} - 1)\mathbf{g}, \quad (1a)$$

$$(\bar{\rho}\mathbb{J} + \mathbb{D}) \cdot \frac{d\boldsymbol{\Omega}}{dt} + \boldsymbol{\Omega} \times [(\bar{\rho}\mathbb{J} + \mathbb{D}) \cdot \boldsymbol{\Omega}] + \mathbf{U} \times (\mathbb{A} \cdot \mathbf{U}) = \boldsymbol{\Gamma}_\omega, \quad (1b)$$

where \mathbf{U} is the velocity of the body center of mass, $\boldsymbol{\Omega}$ is the body rotation rate (i.e., the angular velocity vector), and \mathbb{I} denotes the identity tensor (Mougin & Magnaudet 2002a). The force and torque per unit mass of fluid, \mathbf{F}_ω and $\boldsymbol{\Gamma}_\omega$, result from the existence of vorticity in the flow and do not have a general closed-form expression. The second-order added inertia tensors \mathbb{A} and \mathbb{D} entirely characterize the force and torque resulting from the instantaneous fluid reaction to a translational and a rotational acceleration of the body, respectively. Similar to the body inertia tensor \mathbb{J} , \mathbb{A} and \mathbb{D} depend only on the body geometry and can be computed once and for all for a nondeformable body by considering the short-time response of the flow to a given body acceleration (Magnaudet & Eames 2000, Mougin & Magnaudet 2002a).

When the right-hand side is zero, the system in Equation 1 has been known since Kirchhoff (1869) to generate path oscillations for nonspherical bodies, as the corresponding added mass tensor \mathbb{A} is not isotropic, thus inducing couplings between the force and torque balances (**Figure 2a**); the corresponding paths have been shown to be generally chaotic (Aref & Jones 1993, Kozlov & Onischenko 1982). The vortical loads \mathbf{F}_ω and $\boldsymbol{\Gamma}_\omega$ depend on the entire history of the fluid motion and in general are not fully determined by the degrees of freedom of the body. It is only in some particular situations that they can be modeled as integro-differential operators of \mathbf{U} and $\boldsymbol{\Omega}$, leading, for instance, to the well-known closed-form expression for the unsteady drag on a rigid sphere in the low-Reynolds-number regime (Landau & Lifschitz 1987).

The physical causes of path instability can be separated into two classes. The first class is related to the way the hydrodynamical forces and torques evolve when a disturbance is applied to the body degrees of freedom. An example is given by the oscillations predicted by potential flow theory (**Figure 2a**). However, the corresponding predictions are hardly realistic because the predicted frequency generally differs much from that of the observed path oscillations (it is typically higher by an order of magnitude for light bodies). A similar motion can also be generated when the right-hand sides of the system in Equation 1 involve anisotropic contributions, such as an anisotropic drag, as well as more complex rotational loads, such as those related to a nonzero circulation around the body. The second class involves the wake instability that occurs beyond a critical Reynolds number even if the body is translating with constant speed and orientation. In contrast with the former class, the latter does not require any couplings with the degrees of freedom of the body. However, as soon as flow instability induces a modification of the vortical

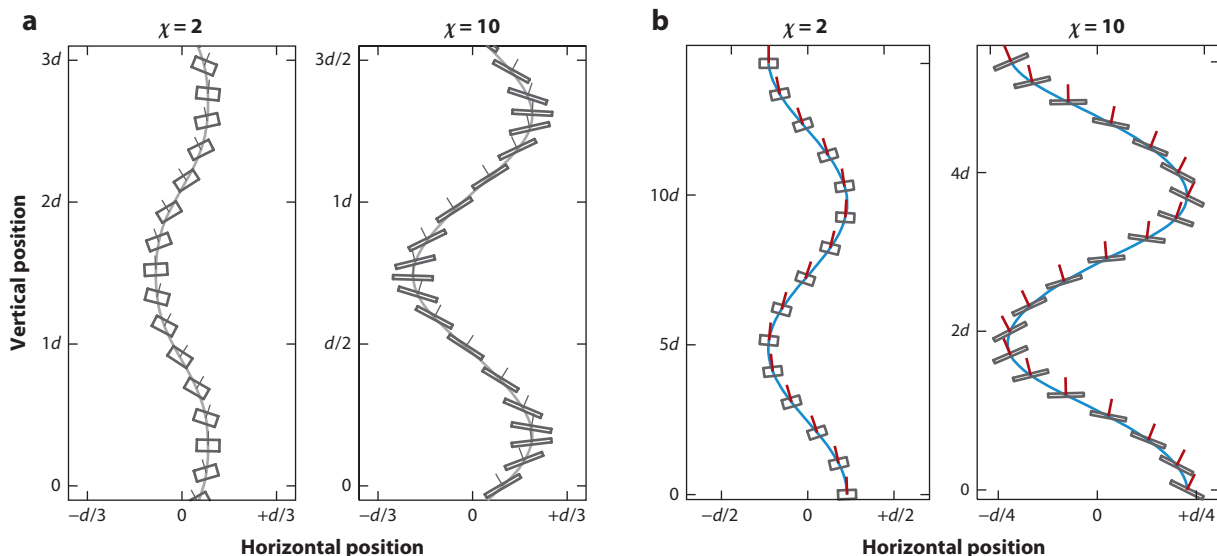


Figure 2

Periodic motion of short cylinders (\equiv thick disks): (a) body contours and paths computed from potential flow theory and (b) experimental contours and paths for $Re = 250$ ($Ar = 90$). The short tick lines indicate the direction of the body symmetry axis. Note that the bodies and paths are drawn with different scales. Figure taken from Fernandes et al. (2005), reprinted with permission from the American Institute of Physics.

efforts \mathbf{F}_ω and $\mathbf{\Gamma}_\omega$, the body motion in turn is altered, and the fluid/body system eventually tends toward a new equilibrium solution satisfying the system in Equation 1. In particular, when an axisymmetric body rises or falls along a straight vertical path, the loss of the axial symmetry in its wake results in the occurrence of asymmetric vortical loads that make it rotate and move sideways. When the Reynolds number is large enough, the wake of any fixed solid body becomes unsteady, and vortices are shed downstream. When such a body is free to move, a modification of the formation and detachment of the vortices (especially of the shedding frequency) is expected. For all bodies discussed here (which are assumed to exhibit spatial symmetry properties and to have a uniform density), path instability turns out to be closely related to the first bifurcation of the wake. An overview of the first wake bifurcations of a fixed body is therefore a prerequisite to a better understanding of the occurrence of oscillatory motions when the body moves freely.

3. WAKE INSTABILITIES OF FIXED BODIES

The most extensively studied scenario of wake transition past a fixed bluff body is certainly that of a long, nominally two-dimensional, circular cylinder held perpendicularly to the incoming flow. As is well known, the wake first becomes unsteady through an absolute instability associated with a Hopf bifurcation at a critical Reynolds number $Re \approx 47$, leading to the shedding of the celebrated von Kármán vortex street at a Strouhal number $St \approx 0.14$ (Re and St are based on the incoming velocity U_∞ , diameter d , and frequency f). The next bifurcation occurs for $Re \approx 190$ and leads to the onset of three-dimensionality. These two steps have been reviewed in detail by Williamson (1996) and in the context of vortex-induced vibrations by Williamson & Govardhan (2004).

Among three-dimensional bodies, the sphere was naturally chosen as a canonical geometry in a number of studies. Modern investigations of wake instability past a fixed sphere started with the

SS: stationary state

global stability analysis of Natarajan & Acrivos (1993) and was succeeded by the DNS of Ghidersa & Dusek (2000), Johnson & Patel (1999), Thompson et al. (2001), and Tomboulides & Orszag (2000) and the detailed experiments of Ormieres & Provansal (1999), which altogether yielded a consistent scenario of the first steps of the transition. In contrast with the circular cylinder, the first bifurcation encountered in the sphere wake is a steady one occurring at $Re = Re_{c1} \approx 212$ [the physical mechanism by which this instability occurs and the reason why its nature is fundamentally different from that of two-dimensional wakes have been explored by Magnaudet & Mougin (2007)]. This bifurcation leads to a stationary state (SS) that is no longer axisymmetric but retains a planar reflectional symmetry with respect to a longitudinal plane passing through the sphere center. The angular orientation of this plane in principle is arbitrary but is generally selected by the holding device in real experiments. Using dye injection (**Figure 3a**), this mode manifests itself through a tilting of the recirculation region and the shedding of two filaments. In DNS (**Figure 3a'**) or in PIV results, its structure is more easily evidenced through the streamwise (or trailing) component

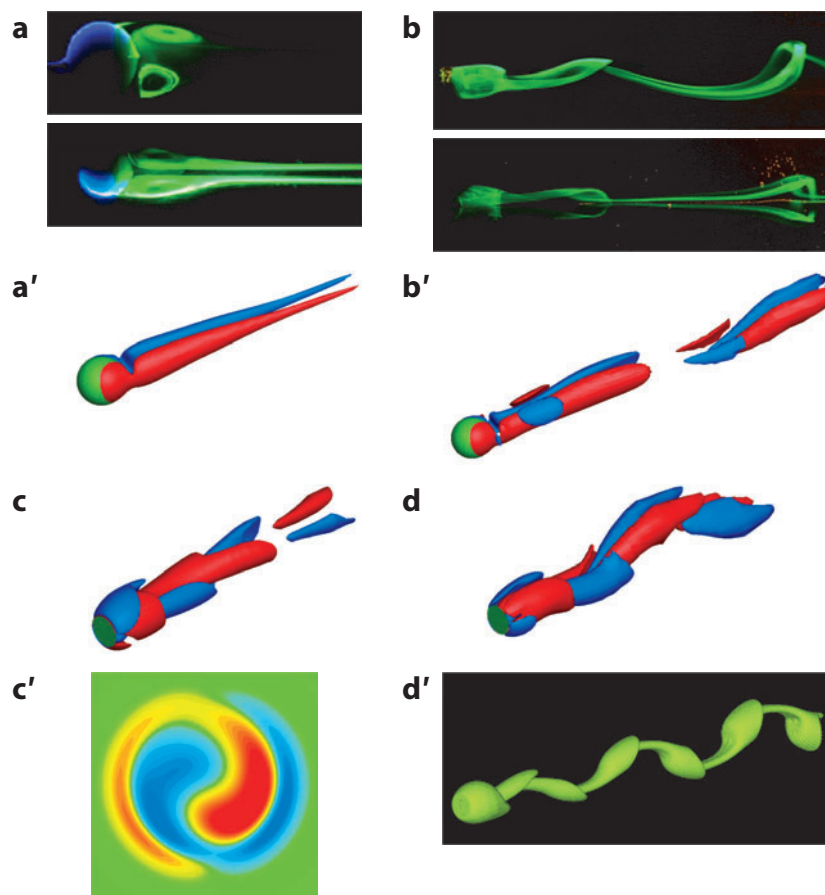


Figure 3

Vortex shedding modes in the wake of a sphere (*a, a', b, b'*) and of an infinitely thin disk (*c, c', d, d'*), illustrated with streamwise vorticity isosurfaces (*a', b', c, d*), streamwise vorticity contours in a cross-plane (*c'*), and experimental (*a, b*) and numerical (*d'*) dye lines. Experiments with a sphere courtesy of A. Prasad and S. Goujon-Durand. Numerical dye lines adapted from Meliga et al. (2009), courtesy of P. Meliga.

of the vorticity, which reveals two steady counter-rotating vortices. (Although the streamwise vorticity component is useful to evidence the symmetries of the wake, it is actually much weaker than the azimuthal component associated with the primary toroidal vortex.) This bifurcated state is also characterized by the existence of a transverse or lift force pointing in a direction contained within the symmetry plane.

A secondary Hopf bifurcation subsequently occurs at $Re = Re_{c2} \approx 273$, leading to a periodic state called reflectional symmetry preserving (RSP) by Fabre et al. (2008) as it retains the symmetry plane selected by the previous bifurcation. This periodic regime is characterized by a Strouhal number $St \approx 0.127$ for $Re \approx Re_{c2}$. Close to the threshold, it manifests itself in small-amplitude peristaltic oscillations of the longitudinal vortices (Gumowski et al. 2008). The oscillations then grow in magnitude, and for $Re \approx 285$, dye lines reveal the shedding of large-amplitude hairpin vortices aligned in the same direction (see **Figure 3b**) (Przadka et al. 2008). The lift force associated with this mode oscillates in magnitude about a nonzero mean, while its direction remains constant. Numerical simulations (**Figure 3b'**) reveal that the wake contains vortical structures of alternating sign and different magnitudes, the weakest ones being invisible in experiments making use of dye injection (Thompson et al. 2001). As the Reynolds number is further increased, a tertiary Hopf bifurcation occurs for $Re \approx 320$ (Bouchet et al. 2006), leading to the occurrence of a secondary frequency about three times smaller than the primary frequency. The wake then becomes irregular but retains a planar symmetry up to $Re \approx 355$, beyond which it becomes fully three dimensional and chaotic (Mittal 1998).

It is worth noting that early dye visualizations performed with liquid drops (Magarvey & Bishop 1961a,b) and rigid spheres (Magarvey & MacLachy 1965) falling in a liquid qualitatively revealed most of the correct transition scenario. In particular, the structure of the first two bifurcated states was correctly captured. The density ratios involved in these experiments were such that the bodies underwent only tiny displacements in the range of Reynolds numbers close to the first two bifurcations, making the results qualitatively relevant to the description of the transition past a fixed sphere.

The infinitely thin disk held perpendicular to a uniform incoming stream is the second axisymmetric body of fundamental interest in the present context. DNS (Fabre et al. 2008) revealed that, whereas the first bifurcation (which takes place at $Re_{c1} \approx 115$) is similar to that of the sphere wake, thus leading to an SS mode with a reflectional symmetry as predicted by Natarajan & Acrivos (1993), the next steps of the transition are qualitatively different. For $Re = Re_{c2} \approx 121$, a secondary Hopf bifurcation occurs. However, unlike the case of the sphere, the resulting state is a reflectional symmetry-breaking mode, associated with a lift force oscillating in direction rather than in magnitude [a similar behavior was also reported for the flow past a hemisphere by Kim & Choi (2003)]. Axial vorticity isosurfaces (**Figure 3c**) show that this mode no longer exhibits planar symmetry but rather consists of vortical structures of opposite signs twisted around each other. Isocontours of axial vorticity in a cross-plane located in the near wake (**Figure 3c'**) reveal a characteristic pattern that led Auguste et al. (2010) to refer to this state as the yin-yang mode. For $Re = Re_{c3} \approx 140$, the flow experiences a third bifurcation, which leads back to a state exhibiting a symmetry plane. However, the corresponding state, referred to as a standing wave mode, differs from the RSP mode because the lift force lies in a different symmetry plane and oscillates about a zero mean. Streamwise vorticity isosurfaces (**Figure 3d**) reveal that the wake then consists of vortical structures of alternating sign but identical magnitude. Dye lines (reconstructed numerically in **Figure 3d'**) reveal large-amplitude hairpin vortices with alternate directions. The next event consists of the emergence of a secondary frequency about three times smaller than the dominant one for $Re \approx 170$, but a truly chaotic and three-dimensional state seems to occur only for $Re \approx 225$ (Auguste 2010).

RSP: reflectional
symmetry preserving

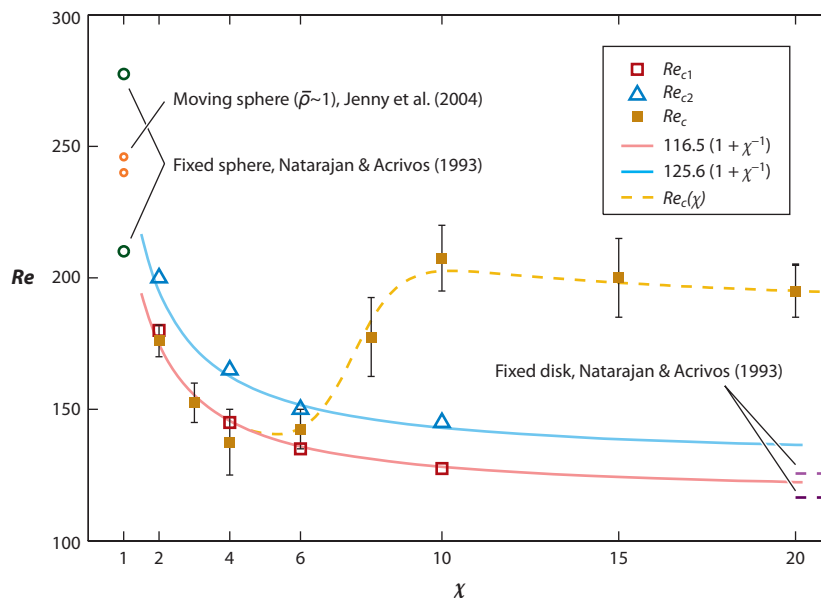


Figure 4

Critical Reynolds numbers characterizing the onset of instabilities of short cylinders of aspect ratio χ . Re_{c1} is the steady bifurcation of the flow past the fixed body (DNS), Re_{c2} is the Hopf bifurcation of the flow past the fixed body (DNS), and Re_c is the onset of the path oscillation of the freely rising body (experiments); the dashed line is an empirical fit of $Re_c(\chi)$. Figure taken from Fernandes et al. (2007), reprinted with permission from Cambridge Univ. Press.

Geometries with intermediate aspect ratios have also been considered. Fernandes et al. (2007) numerically investigated the first two bifurcations of short cylinders (\equiv thick disks) with diameter d , thickness b , and aspect ratio $\chi = d/b$ in the range $\chi \in [2, 10]$ (see **Figure 4**). They showed that, for reasons explained below, the two thresholds can be made independent of χ by introducing a rescaled Reynolds number $Re^* = Re/(1 + \chi^{-1})$. With this renormalization, the first (steady) bifurcation occurs at $Re_{c1}^* \approx 116$, and the second (Hopf) bifurcation occurs at $Re_{c2}^* \approx 126$. Auguste et al. (2010) investigated in detail the bifurcation sequence for a short cylinder with $\chi = 3$ (see **Supplemental Video 1**; follow the **Supplemental Material link** from the Annual Reviews home page at <http://www.annualreviews.org>). This specific geometry turned out to be particularly rich, as all four modes described above are successively encountered, together with a fifth mode with two frequencies and no symmetry plane. An extensive parametric study dealing with oblate spheroids and short cylinders in the range $\chi \in [1, \infty]$, $Re \in [100, 300]$ was recently carried out by Chrust et al. (2011). It basically confirms the findings summarized above and delimits the domain of existence of each state in the (χ, Re) plane. Although the detailed bifurcation sequence greatly varies from one body to another, the first bifurcation always leads to an SS mode with a symmetry plane, and the second bifurcation is always of Hopf type, leading either to an RSP mode (for thick bodies with $\chi \lesssim 4$) or to a reflectional symmetry-breaking mode (for thinner bodies with $\chi \gtrsim 4$).

Theoretical investigations have also recently been carried out to better understand the wake instability of fixed axisymmetric bluff bodies. The linear stability analysis of the axisymmetric base flow [for a rigid sphere and a thin disk (Natarajan & Acrivos 1993) and for a fixed oblate spheroidal bubble (Yang & Prosperetti 2007)] predicts the existence of two unstable eigenmodes

with azimuthal wave numbers $m = \pm 1$. These modes are steady and periodic, respectively, and are clearly associated with the first two bifurcations. However, linear analysis is unable to explain the differences observed in the bifurcation sequence between thin ($\chi \rightarrow \infty$) and thick [$\chi = O(1)$] bodies. In contrast, Fabre et al. (2008) showed that a simple dynamical system of amplitude equations describing the weakly nonlinear interactions of the two leading eigenmodes is able to reproduce the bifurcation scenario for both spheres and disks. A similar dynamical system for the infinitely thin disk was also derived using weakly nonlinear stability analysis and adjoint methods (Meliga et al. 2009), demonstrating remarkable agreement with the DNS results of Fabre et al. (2008). The extension of these ideas to the entire class of body geometries considered in this review is a promising direction of research. However, this approach can apply only to situations in which the first two bifurcations are sufficiently close to each other because the theory on which it leans assumes that the two dominant modes are nearly simultaneously neutral. For thick bodies such as a sphere, this is no longer the case, and a better starting point is to perform a global stability analysis using the three-dimensional, nonaxisymmetric steady state as base flow (Pier 2008).

Although not directly relevant to practical situations, the question of the wake instability of a fixed bubble with a prescribed shape was investigated in detail, in view of its possible connections with the path instability of rising bubbles (Magnaudet & Mougin 2007, Yang & Prosperetti 2007). The problem is also of fundamental interest because of the different nature of the dynamic boundary condition obeyed by the flow at a bubble surface as compared with the usual no-slip condition. Indeed, owing to the usually large viscosity ratio between the outer and inner fluids, and provided no impurity contaminates the interface, the outer flow almost obeys a zero-shear-stress condition at the bubble surface. Therefore, the outer fluid slips along the surface, but vorticity is still generated on it, owing to its nonzero curvature (Batchelor 1967). More precisely, at the surface of an oblate bubble of aspect ratio χ , the maximum vorticity ω_{max} [normalized by the ratio of the upstream velocity over the bubble equivalent diameter $d_{eq} = (6\vartheta/\pi)^{1/3}$, with ϑ denoting the bubble volume] is almost independent of the Reynolds number for large-enough Re (a specificity due to the shear-free boundary condition) but depends critically on χ as $\omega_{max} \propto \chi^{8/3}$ for large-enough χ (Magnaudet & Mougin 2007). The question is then to determine whether and under which conditions this vorticity may lead to an instability in the wake. By performing a series of DNS in which the bubble aspect ratio was progressively increased, Magnaudet & Mougin (2007) found that wake instability first occurs for $\chi = \chi_{cmin} \approx 2.2$ for $Re \approx 500$. When Re and χ are varied independently, the critical curve $Re_c(\chi)$ that bounds the domain within which the flow is unstable exhibits a lower branch $Re = Re_{cl}(\chi)$ and an upper branch $Re = Re_{cu}(\chi)$, with the unstable range $[Re_{cl}, Re_{cu}]$ quickly increasing with the distance to the threshold $\chi - \chi_{cmin}$. Within the unstable range, the first two bifurcated flows correspond to the SS and RSP states found for a rigid sphere. Examination of the variations of the maximum vorticity at the bubble surface along both branches of the curve revealed that the wake becomes unstable when χ (i.e., the bubble oblateness) is large enough for ω_{max} to exceed the threshold $\omega_c \approx 25 + 8.6 \times 10^{-3} Re$. Interestingly, for a solid sphere [at the surface of which $\omega_{max}(Re) \propto Re^{1/2}$], this condition is met for $Re \approx 210$, which corresponds to the threshold of the first, stationary bifurcation.

This correspondence suggests that for the wake to become unstable, a critical amount of vorticity needs to be generated at the body surface, irrespective of the dynamic boundary condition (no-slip versus shear-free) obeyed by the flow. [This proves to be true for two-dimensional wakes as well, as shown by Legendre et al. (2009).] The reason that the aforementioned renormalization by Re^* makes the instability thresholds of short solid cylinders independent of χ is similar, as it was observed that the strength of the vorticity generated at the surface of such bodies essentially behaves as $1/(1 + \chi^{-1})$.

OO: oscillatory
oblique
SO: steady oblique

4. ONSET AND FIRST STAGES OF PATH INSTABILITIES

The body and flow dynamics near the transition from rectilinear motion to path oscillations have been described in several recent studies. The case of a sphere, for which wake instability is the only candidate to generate oscillations, has lately been investigated numerically by Jenny et al. (2004) and experimentally by Veldhuis & Biesheuvel (2007) and Horowitz & Williamson (2010a).

Jenny et al. (2004) observed that the onset of the periodic motion occurs at a Reynolds number, Re_c , higher than that corresponding to the loss of axisymmetry of the wake of a fixed sphere (from now on, Reynolds and Strouhal numbers are based on the mean rise/fall velocity U_m). For light to heavy spheres, Re_c increases (from $Re_c \simeq 224$ for $Ar \simeq 167$ and $\bar{\rho} = 0$) toward the value corresponding to the onset of unsteadiness of the fixed-sphere wake ($Re_c \simeq 273$ for $Ar \simeq 196$ and $\bar{\rho} \rightarrow \infty$). The corresponding Strouhal numbers are close to 0.05 for $\bar{\rho} \leq 2.5$ and to the natural wake frequency $St = 0.127$ for heavier bodies; this abrupt change in St indicates that two unstable modes coexist in this regime, with one of them more (less) unstable than the other for $\bar{\rho} \leq 2.5$ ($\bar{\rho} \geq 2.5$). For all density ratios, the oscillatory oblique (OO) path arises from a steady oblique (SO) path making an angle of approximately 5° with the vertical. This SO path sets in instead of the initial vertical rectilinear path at slightly lower Archimedes numbers ($155 < Ar < 160$, i.e., $205 < Re < 212$, depending on $\bar{\rho}$). In this first nonvertical regime, a slow uniform rotation of the sphere, $\Omega \approx 0.015 V_g/d$, where $V_g = (|1 - \bar{\rho}|gd)^{1/2}$ is the characteristic settling velocity, was also noticed. For light spheres ($\bar{\rho} < 1$), the OO regime becomes rapidly unstable as Ar is increased (typically at $Re \simeq 245$ for $Ar \simeq 180$ and $\bar{\rho} = 0.5$) and is succeeded by a low-frequency periodic path ($St \simeq 0.025$) vertical in the mean, a regime usually referred to as zigzag. All these paths are planar and clearly mirror the SS and RSP states that succeed the first two bifurcations of the fixed-sphere wake. For all density ratios, three-dimensional chaotic paths are subsequently observed in this study at higher Archimedes numbers.

An SO regime associated with a bifid wake and displaying two counter-rotating trailing vortices was also observed for $\bar{\rho} \simeq 2.3$ and $Ar = 176$ by Veldhuis & Biesheuvel (2007) using a Schlieren visualization technique, an observation confirmed in the subsequent PIV measurements of Horowitz & Williamson (2010a). For $Ar = 198$, these two threads of vorticity were found to bend and connect, forming a single-sided chain of vortex rings, as it happens in the wake of a fixed sphere in the RSP regime. This transition and the mean frequency of the subsequent path, $St \approx 0.07$, are in agreement with the findings of Jenny et al. (2004). However, a fourth harmonic ($St \approx 0.25$) was also markedly present in these experiments and became predominant for light spheres ($\bar{\rho} \lesssim 1.3$), at variance with the numerical results. For even lighter spheres ($\bar{\rho} \simeq 0.56$), irregular zigzag paths in which the erratic motion might be interrupted by short transients of periodic zigzag were noticed.

Although experiments suggest that the change in the wake structure that arises at the SO-OO transition barely affects the motion of the sphere, stronger oscillations (with an amplitude of approximately 30% of the mean value for the transverse velocity) are observed in the OO regime in the DNS of Jenny et al. (2004). Increasing the Reynolds number beyond $Re \simeq 260$, Horowitz & Williamson (2010a) noticed that large-amplitude planar oscillations with frequencies about $St \approx 0.06$ occurred through an abrupt, presumably subcritical, transition below a critical density ratio $\bar{\rho} \approx 0.36$. In contrast, for larger $\bar{\rho}$, only oblique paths were noticed and considered rectilinear, as they displayed only irregular low-amplitude transient oscillations (with typical amplitudes $< 0.15 d$ for $\bar{\rho} > 0.5$ and $Re = 450$) associated with a single-sided chain of vortex rings in the wake.

The latter experiments were pursued up to $Re = 1.5 \times 10^4$, and the above sharp transition was always detected, although with two markedly different critical density ratios, namely $\bar{\rho} \approx 0.4$ (0.6) for $260 < Re < 1,550$ ($Re > 1,550$). Interestingly, although the rectilinear paths reported in these experiments and the numerical paths predicted by Jenny et al. (2004) contrast with each other in

their common range of parameters, they also share some similarities, such as the presence of some low-amplitude oscillations superimposed to a dominant mean transverse component. The question therefore arises of the observability in a physical experiment of certain paths predicted for ideal spheres. This point was partly addressed by Jenny et al. (2004), who considered slightly imperfect spheres obtained by displacing arbitrarily the center of mass by $0.025d$ from the geometric center. For $Ar = 170$ ($Re = 235$) and $\bar{\rho} = 0.5$, the path of the nonhomogeneous sphere was found to be oblique and periodic, whereas that of the homogeneous sphere was oblique and steady. For $Ar = 200$ and $\bar{\rho} = 0.5$, the nonhomogeneous sphere displayed a chaotic motion instead of a well-defined zigzag. Also, by performing careful experiments with different levels of residual disturbances in the surrounding fluid, Horowitz & Williamson (2010a) noticed that the observed paths may change dramatically with the background noise. Both series of results reveal the high sensitivity of the body paths to additional effects that are still to be quantified. Especially, in certain ranges of parameters, background noise in the surrounding fluid or a slight deviation from the nominal homogeneity and/or isotropy of the body may have as much of an impact on the observed paths as the loads generated by wake unsteadiness.

Wake instability is again the only candidate for the generation of path oscillations of an infinitely long circular cylinder moving freely in any direction perpendicular to its axis. Namkoong et al. (2008) performed a numerical investigation of this situation for density ratios $0.5 < \bar{\rho} < 4$ and Reynolds numbers between 65 and 185, a regime in which a fixed cylinder wake exhibits periodic two-dimensional vortex shedding. They observed that this shedding induces a small-amplitude periodic motion of the cylinder, in both translation and rotation, with transverse displacements typically lower than $0.1d$. The Strouhal number was found to be a decreasing function of $\bar{\rho}$, with St typically 15% smaller than the Strouhal number St_f of the fixed cylinder for the heaviest body. Vortex shedding occurs when the cylinder is at the mid-point of its transverse motion, a position that also corresponds to the vanishing of the lift force. The cylinder then moves toward its maximum transverse position at which the lift force approaches a maximum; it also rotates about its axis in a direction determined by the cross product of its falling and transverse velocities. By partially restraining the cylinder translation or rotation, Namkoong et al. (2008) showed that the transverse motion of the body plays a crucial role in delaying the onset of vortex shedding and thus reducing the Strouhal number, whereas rotation has a negligible effect.

The observations of Horowitz & Williamson (2006, 2010b) at much higher Reynolds numbers ($3,500 < Re < 7,000$) bear some resemblance to these low-Reynolds-number DNS results. For large-enough density ratios ($\bar{\rho} > 0.54$), only small-amplitude oscillations ($\approx 0.05d$ for $Re \simeq 3,800$ and $\bar{\rho} = 2.0$) at the shedding frequency St_f were detected in these experiments. Both series of paths also share the same wake structure, a periodic von Kármán vortex street (the so-called 2S mode of vortex formation). Owing to the low amplitudes involved, Horowitz & Williamson (2006, 2010b) referred to the path as rectilinear. In contrast, when the density ratio was decreased below the critical value $\bar{\rho} < 0.54$, they noticed the sudden occurrence of a strong oscillatory planar motion with a displacement amplitude of the order of d , a behavior qualitatively similar to their findings with light freely moving spheres.

The wake instability of nonspherical three-dimensional bodies depends strongly on the body aspect ratio, and vortex formation is modified as soon as the symmetry axis of the body (if any) makes some angle with the direction of its velocity. Moreover, nonsphericity plays a crucial role in the left-hand sides of the system in Equation 1, as it makes the generalized inertia tensors $\bar{\rho}\mathbb{I} + \mathbb{A}$ and $\mathbb{J} + \mathbb{D}$ anisotropic and is responsible for the existence of an added mass torque that links the translational and angular velocities of the body. The case of millimetric bubbles rising in water ($\bar{\rho} \simeq 0$), which are known to exhibit path oscillations, is of particular interest because it has long been suspected that bubble shape oscillations coupled with the irrotational mechanisms

► Supplemental Material

leading to the left-hand sides of the system in Equation 1 could be at the root of the phenomenon (e.g., Benjamin 1987; see Magnaudet & Eames 2000 for a more complete historical perspective). Another frequently suggested explanation relied on the role of surfactants, which can prevent the liquid from slipping along the bubble surface, making the bubble qualitatively similar to a light solid body. Joint experimental (Ellingsen & Risso 2001) and computational (Mougin & Magnaudet 2002b) studies have now clarified that the path oscillation of bubbles generally is not driven by shape oscillations, nor by surfactants, but requires only the bubble to be sufficiently oblate for the amount of vorticity produced at its surface to exceed a critical threshold, following the discussion of Section 3 (see **Supplemental Video 2**). DNS (Mougin & Magnaudet 2002b) indicated that path instability occurs when the aspect ratio χ exceeds a value very close to the threshold $\chi_{c_{min}}$ corresponding to the onset of wake instability past a fixed bubble, emphasizing the direct link between wake and path instabilities. An experimental confirmation arose with experiments performed in various silicone oils (Zenit & Magnaudet 2008), in which the onset of path instability was found to coincide with the ω_c criteria indicated in Section 3, once the aspect ratio χ is corrected from the slight fore/aft asymmetry of real bubbles not accounted for in the original model. Mougin & Magnaudet (2002b) noticed that a fixed-shape bubble with $\chi = 2.5$ and $Ar \approx 140$ first follows a rectilinear path and then a planar zigzag, which, after several periods, gradually turns into a helical path, in agreement with experimental observations (Ellingsen & Risso 2001, Shew et al. 2006). By visualizing the wake all along the path, they observed that the onset of the zigzag coincides with the breaking of the axial symmetry in the wake and the birth of a nonzero streamwise component of the vorticity. Similar to the situation of a fixed oblate bubble, the resulting three-dimensional wake structure essentially comprises two counter-rotating vortices but retains a planar symmetry. The appearance of the pair of trailing vortices produces a lift force with a magnitude of the order of the Archimedes force, which in turn induces a sideways motion in the symmetry plane of the wake. The secondary transition from the zigzag to the helical motion is associated with the loss of the planar symmetry.

Fernandes et al. (2007) investigated experimentally the path instability of short cylinders rising or falling with their symmetry axis initially vertical for $\bar{\rho} \simeq 1$ and various aspect ratios $2 \leq \chi \leq 20$. As shown in **Figure 4**, the onset of periodic oscillations of thick cylinders ($2 \leq \chi \leq 4.5$) about the vertical direction (with amplitudes of the order of $0.15d$) coincides with the first bifurcation of the corresponding fixed-body wake ($Re_c \simeq 150$ for $\chi = 3$); the frequency of the subsequent oscillatory motion, $St \simeq 0.12$, is also very close to the natural frequency of the fixed-body wake (**Figure 5**). When the aspect ratio is further increased, so is the critical Reynolds number Re_c corresponding to the onset of path oscillation. In contrast, the critical Reynolds number of the first fixed-body wake instability, Re_{c1} , still decreases with χ (**Figure 4**). In the range $[Re_{c1}, Re_c]$, only small-amplitude erratic motions of the body with short transients of periodic motion at $St \approx 0.12$ were noticed. This behavior was assimilated with a rectilinear motion, as a sharp, presumably subcritical transition to a regime with well-defined quasi-planar oscillations (with an amplitude of approximately $0.25d$ and inclination angles larger than 15°) occurs at a higher Reynolds number, typically $Re_c \simeq 190$ for $\chi \geq 10$. The dynamics of the same bodies was later investigated in detail through DNS by Auguste (2010). Beyond recovering the experimental thresholds and characteristics of the aforementioned oscillatory motions, these DNS also revealed that a whole sequence of complex paths with small-amplitude lateral displacements develops in the intermediate region $[Re_{c1}, Re_c]$, which was not captured experimentally. This issue may again be attributed to the problem of the experimental observability of certain paths that can be predicted only numerically for ideal bodies. We note that the existence of a delayed threshold of path instability was first pointed out by Willmarth et al. (1964), who performed experiments with very thin disks ($\chi \rightarrow \infty$) for which the relative importance of the fluid and disk inertia was measured by the parameter $I^* = \frac{\pi}{64} \bar{\rho} \chi^{-1}$. In

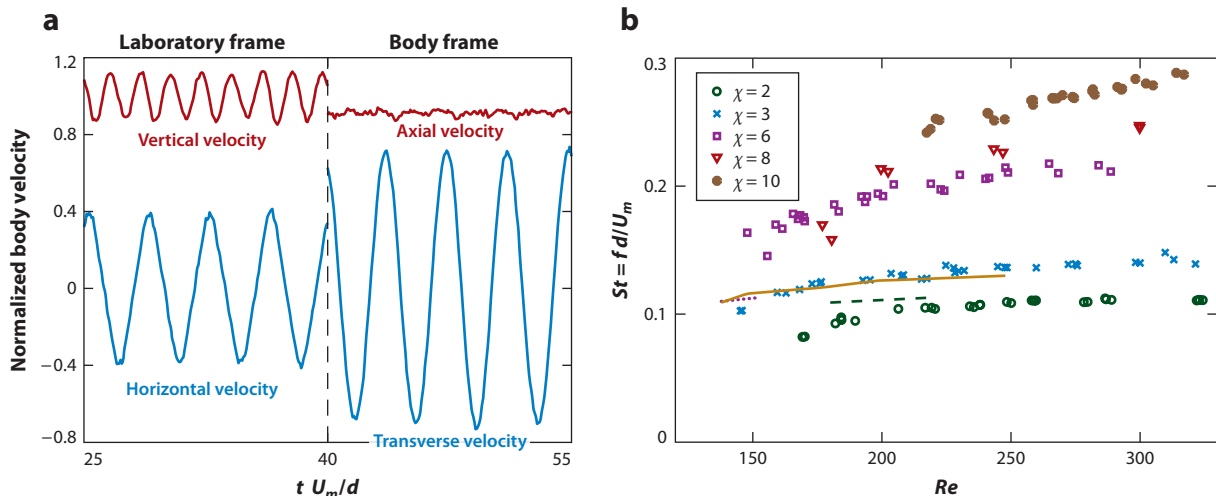


Figure 5

(a) Temporal evolution of the body translational velocity in two different reference frames ($\chi = 10$, $Re = 270$): the laboratory frame (left), with vertical velocity u_V/U_m (blue line) and horizontal velocity v/U_m (red line), and the body frame (right), with axial velocity u_H/U_m (blue line) and transverse velocity v/U_m (red line). (b) Strouhal number versus Reynolds number. The symbols represent experimental data for freely rising cylinders with aspect ratios $\chi = 2, 3, 6, 8$, and 10. The lines are DNS data for the flow about fixed cylinders with $\chi = 2$ (dashed line), 6 (dotted line), and 10 (solid line). Figure taken from Fernandes et al. (2007), reprinted with permission from Cambridge Univ. Press.

these experiments, the onset of significant periodic path oscillations occurred close to the critical Reynolds number of the wake instability of fixed disks, $Re \approx 100$, for large-enough I^* ($\geq 4 \times 10^{-3}$) but was found to be delayed to higher Re for disks of smaller I^* .

5. KINEMATICS AND DYNAMICS OF BODIES ALONG OSCILLATORY PATHS

Particular attention has been paid to the identification of the various paths and wake structures associated with the bodies' oscillations. In a few cases, a quantitative description of the body motion and of the loads acting on it also has been obtained. Different regimes of oscillatory motion now clearly emerge, depending on the nature of the couplings between the body and fluid degrees of freedom. From the situations investigated in the literature, four different regimes of oscillatory motion can presently be outlined. As discussed in the previous section, wake instability is at the origin of nonsymmetric and unsteady loads on the body that, in certain cases, merely result in small-amplitude, possibly irregular or even chaotic, movements of the body. Occurrence of this regime, hereafter denoted as regime A (Figure 6), is described in Section 4. In particular, it has been observed with spheres, nominally two-dimensional cylinders and thin disks, and its detailed investigation is more easily carried out through DNS for the reasons outlined above. A second regime, the B regime (Figure 6), is characterized by regular harmonic oscillations of the body with significant amplitudes. Wake vortices then control the dynamics of path instability, and their evolution is intimately related to the changes in the translational and rotational velocities of the body. A third regime, denoted as regime C (Figure 6), may occur at Reynolds numbers much larger than the threshold of wake instability, when higher-order harmonics become important. Various oscillating paths, more or less regular and possibly chaotic but with still-significant amplitudes, then

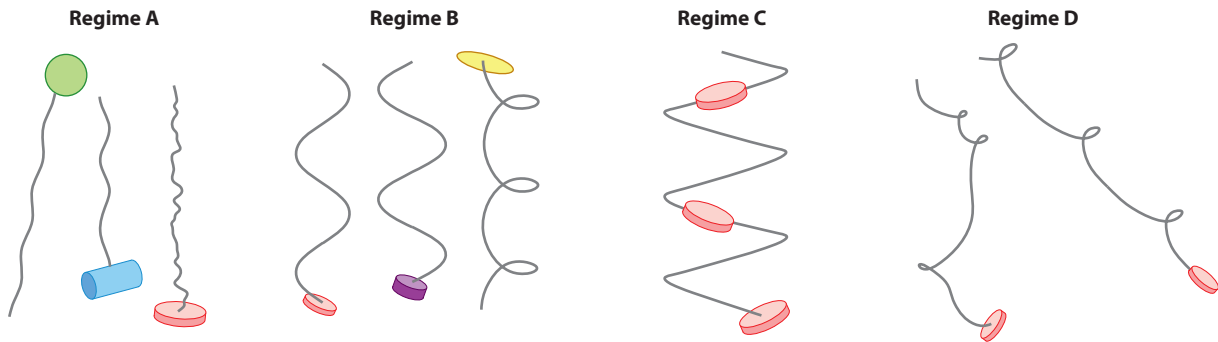


Figure 6

Qualitative picture of the four main regimes of path instability.

develop in conjunction with complex wake structures. In the case of oblate or flat-enough bodies, a highly nonlinear D regime (**Figure 6**) with large rotation rates may also occur at high-enough Reynolds numbers, conveying a markedly different balance of the predominant hydrodynamic loads supporting the oscillatory motions. A reliable marker of regimes B and C as opposed to regime A is the significant increase of the drag coefficient, a well-documented trend for spheres, bubbles, short cylinders, and disks.

This section focuses mostly on regimes B, C, and D for various types of bodies, reviewing the main characteristics of the observed paths and, when available, the loads that support them and the corresponding predictive dynamical models.

5.1. Long Cylinders and Spheres

The dynamics of the sphere beyond $Re \approx 250$ is far from being fully understood, but the variation of the drag coefficient $C_D(\bar{\rho}, Re)$ provided by the three available studies conveys insightful information (C_D is based on the apparent weight, vertical mean velocity, and cross-sectional area of the body). In the DNS of Jenny et al. (2004), the drag coefficient of spheres corresponding to density ratios $\bar{\rho} \geq 0.5$ follows the standard drag law throughout the entire range of Re investigated ($Re \leq 550$, approximately). In contrast, for $\bar{\rho} = 0$ (no intermediate value of $\bar{\rho}$ was considered in this study), C_D almost stops decreasing for $Re > 300$ and keeps a value close to 0.65. A qualitatively similar behavior was reported by Veldhuis et al. (2009) at higher Reynolds numbers, typically $900 \leq Re \leq 2 \times 10^3$. No deviation from the standard drag curve was observed for $\bar{\rho} \geq 0.3$, but, despite significant scatter in the results, the drag coefficients of very light spheres with $\bar{\rho} = 0.02$ (which have oscillating paths with an amplitude about the sphere diameter) were found to take an almost constant value, $C_D = 0.85 \pm 0.15$. The findings of Horowitz & Williamson (2010a), who covered a much broader range of Reynolds numbers, are qualitatively similar: Spheres corresponding to density ratios larger than the critical $\bar{\rho}_c$ of the abrupt transition they detected for $Re > 260$ follow the usual drag law, whereas the drag coefficient of lighter spheres [i.e., those corresponding to $\bar{\rho} \leq 0.36$ (0.6) for $Re \leq 1,550$ ($>1,550$), which have oscillating paths with an amplitude of approximately $0.75d$] is almost constant and close to 0.75 throughout the entire range of Reynolds numbers. Therefore, although the terminology employed by the various groups to qualify the observed paths is different, a qualitatively consistent picture emerges from these three investigations for Reynolds numbers larger than Re_c : Beyond a critical density ratio $\bar{\rho}_c$, they all indicate barely a change in the drag coefficient, a probable signature of an A regime. In contrast, path oscillations are much larger for $\bar{\rho} \leq \bar{\rho}_c$, corresponding to a B or a C regime (depending on

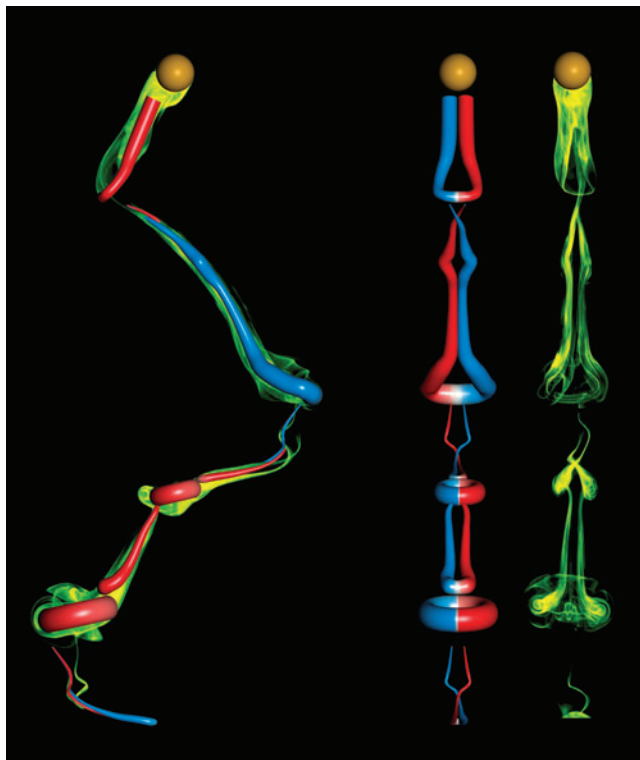


Figure 7

Visualization of the 4R-vortex mode in the wake of a light zigzagging sphere by a combination of dye lines and PIV-based reconstruction of the isosurface $\omega d/U_m = \pm 0.2$ of the streamwise vorticity. Figure taken from Horowitz & Williamson (2010a), reprinted with permission from Cambridge Univ. Press.

the distance $Re - Re_c$), and they result in a marked increase in C_D , which is typically twice as large as the fixed-sphere value for $Re > 10^3$. The discrepancies in the reported paths and most probably on the value of $\bar{\rho}_c$ suggest that the case of the sphere, which is singular owing to its point-symmetric character, is sensitive to tiny imperfections in the body mass distribution or to minute errors in the simulations.

The dye visualizations and PIV measurements of Horowitz & Williamson (2010a) reveal that in these B and C regimes, which in their experiments correspond to periodic zigzagging paths, the wake is unsteady with four hairpin vortices generated per cycle of body motion (the so-called 4R mode; see **Figure 7**). A periodic streamwise oscillation with a typical amplitude $0.1\text{--}0.15d$ at a frequency twice that of the transverse motion is also noticed and shown to be responsible for the existence of the secondary vortex ring generated every half-period. Moreover, the sphere undergoes a significant periodic rotation with an angular amplitude and acceleration of approximately 15° and $0.2(V_g^2/d)$ for $Re = 450$, respectively.

Horowitz & Williamson (2010b) also identified a C regime of nominally two-dimensional cylinders, qualitatively similar to the above B and C regimes of the sphere for $3 \times 10^3 \leq Re \leq 7 \times 10^3$ and density ratios less than $\bar{\rho} = 0.54$, a critical value at which they noticed the sudden occurrence of a strong oscillatory planar motion (with displacement amplitudes of the order of d) accompanied by a jump in the main frequency (approximately 1.3 times smaller than St_f) and a change in the wake structure, with two vortex pairs generated per cycle (the 2P mode of vortex formation). In this

regime, the transverse displacement oscillation exhibits a significant third harmonic. Typically, for $Re = 3,800$ and $\bar{\rho} = 0.45$, the amplitude of the transverse motion is $A_y \simeq d$, but the body also oscillates vertically with an amplitude $A_x \simeq 0.3d$, the phase lag between the two motions being 45° , which corresponds to an upstream displacement when the body reaches its maximum transverse position.

5.2. Bubbles

When wake instability sets in, the bubble velocity is provisionally not aligned with its symmetry axis anymore. Then the wake-induced and added mass torques combine to induce its rotation and initiate its periodic motion, which is first contained within the plane of the trailing vortices, as revealed by the experiments of Lunde & Perkins (1997) and de Vries et al. (2002). Owing to the time-dependent asymmetry of the fluid velocity distribution induced by the rotation, the sign of the trailing vorticity reverses every half-period of motion (Mougin & Magnaudet 2002b, Zenit & Magnaudet 2009). In contrast, the trailing vorticity never changes sign during the subsequent helical regime within which the bubble rotates at a constant rate: In this regime, the two vortices wrap up around one another in such a way that the wake structure becomes stationary in a reference frame attached to the bubble. For both zigzag and helical paths, crest-to-crest amplitudes of the transverse motion and maximum inclination angles reported in the literature vary in the ranges $3-5d_{eq}$ (where d_{eq} is the equivalent diameter defined in Section 3) and $20^\circ-30^\circ$, respectively, and the frequency of the transverse motion lies in the range $0.09 \leq St \leq 0.15$ (Mougin & Magnaudet 2002b). Therefore, these paths clearly correspond to a B- or C-type regime. A key feature of the kinematics of spheroidal bubbles is that the bubble velocity and minor axis are almost aligned along the whole path (Ellingsen & Risso 2001). This was confirmed in the DNS of Mougin & Magnaudet (2002b) in which the drift angle between the velocity and orientation directions was found to oscillate with an amplitude less than 2° . The axial bubble velocity component is nearly constant, whereas the transverse velocity and inclination angle oscillate at the same frequency and nearly in phase. The rise velocity has been consistently reported to decrease, corresponding to an increase of the drag, during the rectilinear/zigzag and zigzag/helix transitions, although this trend is less salient in experiments (e.g., Shew et al. 2006) than in DNS assuming a prescribed bubble shape, presumably because of the slight deformation undergone by real bubbles during each transition.


The various forces and torques acting along the zigzag and helical paths were computed from DNS data by Mougin & Magnaudet (2006) and from experimental data (assuming a zero drift angle at any time) by Shew et al. (2006), allowing for a detailed analysis of the corresponding balances. When a planar zigzag takes place in the vertical (x, y) plane, with x (y) parallel (perpendicular) to the bubble symmetry axis, the vortical loads on the right-hand sides of the system in Equation 1 reduce to the axial and transverse vortical forces, $F_{\omega x}$ and $F_{\omega y}$, and to the vortical torque, Γ_ω , which acts in the z direction perpendicular to the plane of motion. $F_{\omega y}$ and Γ_ω change sign every half-period, slightly after the bubble crosses the inflection point of its path, a direct consequence of the temporal evolution of the vorticity in the trailing vortices. The vortical force $F_{\omega y}$ is at leading order balanced by the y component of the buoyancy force and of the centripetal added mass force $\mathbf{\Omega} \times (\mathbf{A} \cdot \mathbf{U})$, which are 90° out of phase. Hence $F_{\omega y}$ determines the maximum of both the inclination angle of the path and the bubble rotation rate. The vortical torque is almost balanced by the restoring added mass torque $\mathbf{U} \times (\mathbf{A} \cdot \mathbf{U})$, which results from the geometrical anisotropy of the bubble, and this balance generates a small but nonzero transverse velocity. As the path is symmetric and vertical on average, $F_{\omega x}$ oscillates at a frequency twice that of $F_{\omega y}$ and Γ_ω , with the amplitude of these oscillations typically an order of magnitude less than those of $F_{\omega y}$. Once the helical motion is established, the bubble reaches a constant rise velocity, and $F_{\omega x}$ keeps a constant

value, which balances the streamwise buoyancy force. The main difference with the zigzag regime is that the centripetal added mass force and the transverse component of the buoyancy force now act in two perpendicular directions y' and z' corresponding to the normal and binormal to the path, respectively. As a result, the y' component of \mathbf{F}_ω determines the bubble rotation rate, whereas its z' component determines the pitch angle of the path.

5.3. Short Cylinders and Disks

A similar balance of hydrodynamical loads governs the B regime of solid short cylinders in the ranges of parameters $2 \leq \chi \leq 10$, $80 \leq Re \leq 350$, and $\bar{\rho} \approx 1$ (Fernandes et al. 2008) (see **Supplemental Video 3**). The corresponding oscillatory motions consist of helical paths of low helicity that, at leading order, can be considered planar zigzags (Fernandes et al. 2007). The main differences with the case of oblate bubbles are that the transverse force balance now also involves the body inertia through the centripetal contribution $\bar{\rho}\boldsymbol{\Omega} \times \mathbf{U}$ and that the transverse velocity required to balance the vortical torque is much larger, owing to the smaller rise velocity allowed by the small density contrast $|\bar{\rho} - 1|$. Also, a stronger vortical torque is observed for thin bodies, resulting in larger transverse velocities and thus in a larger drift angle between the symmetry axis and the velocity of the body. The aspect ratio deeply influences the characteristics of the motion in this regime. Indeed, as shown in **Figure 5**, the Strouhal number evolves as $\chi^{1/2}$ and is much smaller than the prediction provided by potential flow theory regardless of χ 's value; in contrast, St depends only weakly on Re . For $\chi = 3$, St is close to the natural frequency of the fixed-body wake ($St \approx 0.12$), but for thinner bodies ($\chi = 10$), it is almost three times larger (see **Supplemental Video 4**). Moreover, the relative phase $\Delta\phi$ between the oscillations of the horizontal velocity and those of the body inclination also strongly depends on χ (see **Figure 2b**) and barely evolves with Re (Fernandes et al. 2005, 2007; Shenoy & Kleinstreuer 2010). These oscillations are nearly in phase for thick bodies ($\chi \leq 4$), the symmetry axis then being nearly tangent to the path as it is during the zigzag motion of spheroidal bubbles. As χ increases, so does $\Delta\phi$, which exceeds 90° for thin bodies ($\chi \geq 8$), so that these bodies seem to glide along their path, reaching their maximum inclination at the turning points (see **Supplemental Video 5**). This behavior is reminiscent of the fluttering motion of thin plates and falling leaves. We note that a similar continuous evolution of $\Delta\phi$ was observed with oblate spheroids having aspect ratios ranging from 1.8 to 4.8 (Fernandes et al. 2005). In contrast to $\Delta\phi$, the amplitude of the transverse velocity oscillations and that of the inclination oscillations strongly depend on both χ and Re . Normalizing the transverse velocity with the characteristic scale ωd (where ω is the radian frequency of the body oscillations) and introducing again the Reynolds number Re^* accounting for the production of vorticity at the body surface (see Section 3), we see that both amplitudes fall on a master curve that depends only on Re^* (Fernandes et al. 2007).

The chronology of the forces and torques acting on the body in connection with the wake dynamics has been analyzed using PIV (Ern et al. 2007). Different vortex formation and shedding processes were found to be related to the different types of motion observed as χ changes. The differences arise from the fact that the problem is governed by two independent timescales. On the one hand, the oscillatory motion and the vortex shedding process are characterized by the timescale $\tau_o = 2\pi\omega^{-1}$. On the other hand, the evolution of the vortices in the wake is governed mostly by the advective timescale $\tau_i = d/U_m$. In particular, the phase difference between the transverse vortical force $F_{\omega y}$ and the torque Γ_ω scales with τ_i , regardless of the values of χ and Re . For thick bodies, the ratio of these two timescales is merely the Strouhal number of the corresponding fixed-body wake, whereas for thinner bodies, τ_i becomes much larger than τ_o . Using these ideas, Ern et al. (2009) developed a dynamical model that reproduces the various periodic zigzag motions

 **Supplemental Material**

of axisymmetric bodies over a wide range of χ . The model is made of a differential equation and an integro-differential relation that complement the system in Equation 1. The former equation models the growth and saturation of the oscillatory vortical force and torque by considering them oscillators with a characteristic time τ_o to mimic the effect of the periodic vortex shedding. In contrast, their amplitudes are assumed to evolve on the longer timescale τ_i , which allows the transient motion of the bodies after their release to be properly recovered. The second equation accounts for the effect of the body rotation on the vortical loads, taking the form of a relation between $F_{\omega y}$ and Γ_{ω} , which depends on the body rotation rate and is consistent with the fixed-body case. This equation yields a phase difference between $F_{\omega y}$ and Γ_{ω} , driven by the history of the body rotation rate, which produces the observed deviation from the fixed-body behavior when χ increases.

Other types of motion have been identified at higher Reynolds numbers with thin disks (in practice, $\chi \geq 10$), depending on the dimensionless moment of inertia $I^* = \frac{\pi}{64} \bar{\rho} \chi^{-1}$. In the case of small I^* (typically $< 10^{-2}$), Zhong et al. (2011) observed that the planar periodic motion is not stable and that a secondary oscillation grows in the normal direction, leading to a fully helical path for small-enough values of I^* (typically $< 10^{-3}$ but depending on Re). These paths correspond to a C regime in the range of Re that was considered, but a helical motion may exist in the B regime at lower Re . Whereas a periodic shedding of hairpin vortices accompanies the planar periodic path (Willmarth et al. 1964), Zhong et al. (2011) showed that the helical path is related to the continuous shedding of a helicoidal vortex. Moreover, they observed that the helical path is associated with a rotation of the body about its symmetry axis, with the corresponding angular velocity about half those in the transverse directions. For moderate I^* ($9 \times 10^{-3} \leq I^* \leq 4 \times 10^{-2}$), Stringham et al. (1969) and Field et al. (1997) observed that the periodic motion becomes chaotic, a large-amplitude, back-and-forth lateral motion alternating with some periods of tumbling (see **Supplemental Video 6**). For I^* larger than 4×10^{-2} and large-enough Re , the tumbling regime sets in, and the disk starts to turn continuously end-over-end while drifting horizontally. Unfortunately, almost no quantitative information concerning the body kinematics and dynamics is available in these regimes, except to some extent from the high-Reynolds-number ($2.2 \times 10^3 < Re < 4.4 \times 10^3$) experiments of Stewart & List (1983) performed with short cylinders ($\chi = 3.6$) in the range $0.4 < I^* < 1.5$. However, these regimes display strong similarities with those observed with thin plates, which we now describe.

5.4. Nominally Two-Dimensional Plates

Since the early remarks of Maxwell (1853), the various oscillatory regimes of nominally two-dimensional falling plates (with thickness b , width d , and thickness-to-width ratio $\chi = d/b$) have received a great deal of attention in a range of parameters far from the onset of the periodic motion. The path generally referred to as fluttering (**Figure 8a**), which is vertical in the mean, corresponds to a behavior qualitatively close to that of the short cylinder with $\chi = 10$, shown in **Figure 2b**. As its dimensionless moment of inertia I^* is increased [$I^* = k \bar{\rho} \chi^{-1} (1 + \chi^{-2})$, where k depends on the geometry of the cross section], the plate begins to tumble (**Figure 8c**): When its inclination angle reaches 90° , the body proceeds to complete a whole turn, while drifting in the mean in an oblique direction.

The fluttering and tumbling regimes of freely falling nearly two-dimensional plates and cards have been investigated experimentally by Smith (1971), Belmonte et al. (1998), and Mahadevan et al. (1999) who checked that the Strouhal number $St = f_T d / V_g$ associated with the tumbling frequency f_T is constant, with now $V_g = [(\bar{\rho} - 1)gb]^{1/2}$ and in more detail by Andersen et al. (2005b) with $\bar{\rho} \approx 2.5$, $5 \leq \chi \leq 14$, and $Re = O(10^3)$ (**Figure 8**). Similar to the findings of Field et al. (1997) with thin disks, Andersen et al. (2005b) observed that the tumbling motion may become

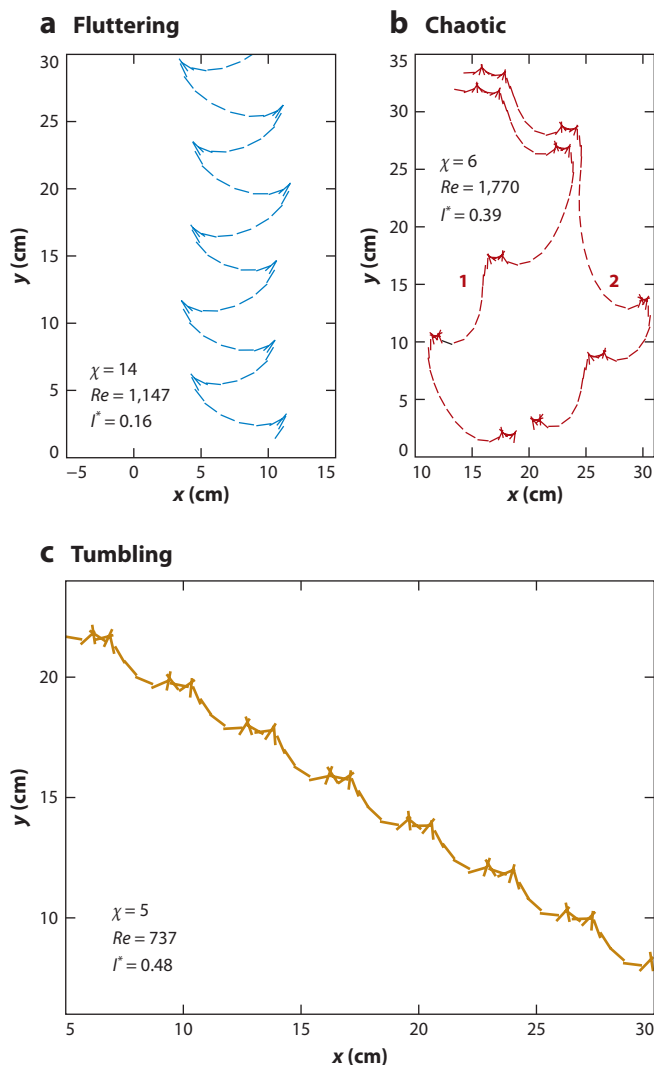


Figure 8

Three contrasted paths observed with nominally two-dimensional plates: (a) fluttering, (b) two apparently chaotic paths obtained with the same plate, and (c) tumbling. The line segments show the plate's cross section. Figure taken from Andersen et al. (2005b), reprinted with permission from Cambridge Univ. Press.

chaotic for large-enough I^* and Re (see **Figure 8b**). A noticeable feature of this regime (which may also happen in the fluttering regime close to the transition to tumbling) is that the center of mass of the plate may rise during some time after the long gliding stage preceding each turning point of the path. This elevation, confirmed by the two-dimensional DNS of Pesavento & Wang (2004) and Andersen et al. (2005a), is accompanied by a deceleration of the plate, which makes the near wake unstable and forces it to break up into separate vortices of size $\approx d/2$. Moreover, the boundary layers attached to the upper and lower surfaces of the plate detach at each turning point, leading to the shedding of a pair of counter-rotating vortices. These wake dynamics clearly involve a synchronization of vortex shedding and body rotation and have close connections with

those encountered in the autorotation of wings about a fixed axis, a situation investigated both experimentally (Smith 1971) and numerically (Lugt 1980, Mittal et al. 2004) and reviewed by Lugt (1983).

The force and torque balances in Equation 1 were analyzed by Andersen et al. (2005b), using experimental and DNS data. As in the case of short cylinders and bubbles, the restoring added mass torque provides a much larger contribution to Equation 1b than the term proportional to the rotational acceleration. In contrast, the axial and transverse force balances in Equation 1a strongly differ from those discussed in the previous sections. This is because, for the set of parameters investigated in the aforementioned references, nonlinear effects are crucial, and higher-frequency harmonics cannot be ignored: Clearly these situations belong to the C and D regimes. When the plate flutters, its transverse velocity is about three times larger than its mean settling velocity, whereas when it tumbles, it follows a path inclined at approximately 35° – 45° to the vertical so that both velocity components are comparable. In such situations, the transverse linear acceleration of the body provides a dominant contribution to the transverse force balance, whereas the added mass terms appear negligible.

There have been several attempts to develop an empirical but realistic model of the vortical forces and torques capable of predicting the observed features of the fluttering and tumbling regimes as well as the corresponding transition. The two key ingredients common to all models to date are a quasi-steady dissipative contribution (i.e., a drag force and a torque opposing rotation) and a quasi-steady lift contribution. Models differ in the expression of these forces and torques with respect to the kinematic degrees of freedom. In earlier versions, the circulation either was given an arbitrary constant value (Mahadevan 1996) or was attributed the value predicted by the Kutta-Joukowski theorem (Belmonte et al. 1998, Tanabe & Kaneko 1994). The dissipative contribution was assumed to be linear with respect to the body translational and rotational velocities, i.e., to originate directly from viscosity (Tanabe & Kaneko 1994), to be quadratic, i.e., governed by inertia (Belmonte et al. 1998), or both (Mahadevan 1996), with direction-dependent drag coefficients in all cases. For some combination of the model parameters, the anisotropy of both the translational added mass coefficients and the drag coefficients results in a saddle-node bifurcation that corresponds to the transition from fluttering to tumbling (Mahadevan 1996). In the most recent versions of these models (Andersen et al. 2005b, Pesavento & Wang 2004), the circulation is assumed to depend in a nonlinear manner on the translational velocity so as to take stall into account when the inclination of the plate is large. More importantly, it also comprises a contribution that depends linearly on the rotational velocity, the role of which was found crucial for reproducing the elevation of the plate near the turning points (Pesavento & Wang 2004). Finally, the model involves a single drag coefficient assumed to depend nonlinearly on the inclination angle. The complete model makes use of a total of six adjustable parameters that need to be fitted with respect to reference situations. Another complementary viewpoint was provided by Jones & Shelley (2005) who, using a boundary integral technique, computed the first stages of the two-dimensional inviscid flow past a fluttering plate released from rest. They showed that unsteady vortical loads arising from the relative motion between the plate and its wake play a dominant role in the dynamics of the coupled system. As such loads cannot be related to the body translational and rotational velocities in a quasi-steady manner, their findings question the generality of the semiempirical models discussed above.

6. CONCLUDING REMARKS AND OPEN QUESTIONS

In this review we attempt to present the current state of understanding of the path oscillations of freely moving bodies and of their connections with the dynamics of the body wake. Although

many studies are still under way, and the current coverage of the parameter space of **Figure 1** is still extremely uneven, tremendous progress has been achieved on the subject, essentially during the past decade. We think that the main points of consensus may currently be summarized as follows.

The onset of the path instability of a given body within a viscous fluid is closely related to the onset of the instability of the fixed-body wake, and the corresponding two critical Reynolds numbers are close. The kinematics and dynamics of the first path departing from the initial vertical trajectory reflect that of the first unstable wake mode. Therefore, wake instability turns out to be a necessary condition for path instability to occur. Nevertheless, this condition is not always sufficient for the body to display experimentally discernible lateral displacements for Reynolds numbers slightly beyond the threshold. In particular, spheroidal bodies and short cylinders with moderate aspect ratios (typically $\chi \leq 6$) do, but thinner cylinders closer to the thin-disk limit $\chi \rightarrow \infty$ exhibit a significant range of Reynolds numbers we call the A regime, within which only tiny, mostly erratic, movements are detected.

The magnitude of the vorticity produced at the body surface by the no-slip or the shear-free boundary condition (for bubbles) appears to be a key quantity to predict the onset of the wake instability of fixed bodies. More precisely, once properly reexpressed using a criterion based on this quantity, such as the Reynolds number Re^* for short cylinders or the ω_c criterion for spheroidal bubbles and rigid spheres, the threshold of the first instability becomes independent of the nature (no-slip versus shear-free) of the body surface and of the body aspect ratio within a given family of shapes (e.g., spheroids, short cylinders). Consequently, the magnitude of the surface vorticity is also relevant to the prediction of the onset of path instability when it almost coincides with that of wake instability, i.e., for bodies that go directly from straight vertical paths to a B regime of oscillations.

A comparison of the behavior of the various three-dimensional bluff bodies considered here, including bubbles, indicates that for a given Archimedes number and body shape, the magnitude of the lateral body movements increases as the density ratio decreases, although there are still disagreements, especially for the sphere, on the critical $\bar{\rho}$ below which a clear B regime sets in. The role of the body anisotropy is more subtle, as this factor is in particular responsible for added mass effects that couple the translational and rotational body velocities, so that weakly anisotropic bodies move with their short axis almost perpendicular to the path, whereas flat bodies tend to glide along it.

Depending on the distance $Re - Re_c$ to the threshold, there exists a broad range of situations, from those, close to the threshold, in which the body lateral movements essentially reflect the wake dynamics and barely modify them (e.g., the sphere for $Re \gtrsim Re_{c,2}$), to those, far from the threshold and hence corresponding to the C and D regimes, in which the wake is unstable anyway and the body path drives the vortex shedding dynamics (e.g., the tumbling of nearly two-dimensional plates). In the latter two regimes, it is not yet clear whether every new bifurcation of the wake encountered as Re increases leaves a footprint on the path. The question is especially relevant for strongly anisotropic bodies as in this case the connection between path and wake instabilities is far from straightforward in those regimes, owing to the ability of such bodies to oscillate on their own with a natural frequency that may greatly differ from that of the wake.

Before ending with some suggestions for future research, we stress that the problem is demanding, whatever methodology is used to tackle it. Laboratory experiments require extreme care to control the residual motions in the surrounding fluid and to reduce undesired inhomogeneity in the body. DNS requires the development of specific algorithms capable of solving properly the coupled body-fluid problem and of dealing with the outflow boundary condition, both with an accuracy compatible with the usual requirements of stability problems. In particular, few techniques,

based mostly on boundary-fitted grids, address the first item satisfactorily enough to allow an exploration of the initial stages of path instability (e.g., Jenny & Dusek 2004, Mougin & Magnaudet 2002a). Finally, theoretical stability analyses of the coupled fluid-body problem combine the usual difficulties of stability studies in strongly nonparallel flows with the presence of the new degrees of freedom and hence the new eigenmodes brought by the body (Fabre et al. 2011). Despite these intrinsic difficulties, the challenge is worth taking up to address the most important questions that are still open and to fill the gap between some of the most different situations investigated to date. In our view, future efforts should focus especially on the following issues.

A systematic exploration of the parameter space is clearly missing. Although it is certainly not worth covering the whole space, a reasoned exploration is required to fully understand the effect of each control parameter of the system and the specificities related to each family of geometries. This exploration should be based on a suitable combination of detailed laboratory experiments and DNS, which, provided the numerical technique satisfies the criteria mentioned above, is currently more efficient to deal with situations involving tiny body displacements, especially the A regime. Some situations are also probably worth revisiting to resolve current controversies (e.g., light spheres close to the threshold between regimes A and B).

Linear and weakly nonlinear stability studies including the body degrees of freedom are still in their infancy. Although what can be learned from them is limited to the neighborhood of the threshold, they are the right tool to get a clear view of the nature of the first unstable modes, of the underlying physical mechanisms, and on the way these modes interact to produce new wake and path structures. Despite their limited range of validity, they may also be suitable guides to build models on rational bases.

The mechanisms by which the geometry and frequency of path oscillations are selected are not properly understood in a number of cases. This is especially clear in, but not limited to, situations in which no real vortex shedding takes place, such as bubbles followed by a double-threaded wake. In such a situation, why is, for instance, a periodic zigzag motion, vertical in the mean, selected instead of an oblique path? Well-defined helical paths (such as those observed with bubbles or disks in certain regimes) also raise specific questions, as they do not directly result from the spatial organization of the fixed-body wake at the corresponding Reynolds number but rather from the intimate couplings between the wake and an already oscillating path. The way the transition to such paths occurs, especially the nature of the corresponding bifurcation(s), and the reorganization of the wake dynamics it implies are mostly unknown presently and need to be clarified.

The quest for general low-order models capable of predicting the observed paths over a wide range of Reynolds numbers, body geometries, and density contrasts should be actively pursued. Although such models will probably always involve a few adjustable parameters, the fundamental question is now to determine the content and minimum number of physically relevant ingredients that they should contain, as well as their mathematical structure, especially to go beyond the quasi-static assumption of most of the approaches available to date. Such models will probably involve additional differential equations to mimic the wake dynamics.

Finally, future work will need to consider situations of higher complexity than the motion of a single body in an unbounded fluid at rest at infinity, which has been the common framework of all studies reviewed here. Practical situations frequently involve the presence of walls, the existence of an inhomogeneous underlying flow, and the coexistence of several or even many bodies close to each other. In such situations, several interaction mechanisms may dramatically modify the conditions for path instability to occur and alter the subsequent body paths. They need to be carefully investigated and accounted for in future models.

DISCLOSURE STATEMENT

The authors are not aware of any biases that might be perceived as affecting the objectivity of this review.

ACKNOWLEDGMENTS

We are indebted to Sophie Goujon-Durand and Adam Przadka, Philippe Méliga, Jane Wang, and Charles Williamson, who generously provided graphical material to illustrate this review, and to the many colleagues and students who over the years shared their views with us on this fascinating subject.

LITERATURE CITED

- Andersen A, Pesavento U, Wang ZJ. 2005a. Analysis of transitions between fluttering, tumbling and steady descent of falling cards. *J. Fluid Mech.* 541:91–104
- Andersen A, Pesavento U, Wang ZJ. 2005b. Unsteady aerodynamics of fluttering and tumbling plates. *J. Fluid Mech.* 541:65–90
- Aref H, Jones SW. 1993. Chaotic motion of a solid through ideal fluid. *Phys. Fluids A* 5:3026–28
- Augsburger CK. 1986. Morphology and dispersal potential of wind-dispersed diaspores of neotropical trees. *Am. J. Bot.* 73:353–63
- Auguste F. 2010. *Instabilités de sillage générées derrière un corps solide cylindrique, fixe ou mobile dans un fluide visqueux*. PhD thesis. Univ. Paul Sabatier, Toulouse
- Auguste F, Fabre D, Magnaudet J. 2010. Bifurcations in the wake of a thick circular disk. *Theor. Comput. Fluid Dyn.* 24:305–13
- Batchelor GK. 1967. *An Introduction to Fluid Dynamics*. Cambridge, UK: Cambridge Univ. Press
- Belmonte A, Eisenberg H, Moses E. 1998. From flutter to tumble: inertial drag and Froude similarity in falling paper. *Phys. Rev. Lett.* 81:345–48
- Benjamin TB. 1987. Hamiltonian theory for motion of bubbles in an infinite liquid. *J. Fluid Mech.* 181:349–79
- Bouchet G, Mebarek M, Dusek J. 2006. Hydrodynamic forces acting on a rigid fixed sphere in early transitional regimes. *Eur. J. Mech. B* 25:321–36
- Burrows FM. 1975. Wind-borne seed and fruit movement. *New Phytol.* 75:405–18
- Chrust M, Bouchet G, Dusek J. 2011. Parametric study of the transition scenario in the wake of oblate spheroids and flat cylinders. *J. Fluid Mech.* 665:199–208
- de Vries A, Biesheuvel A, van Wijngaarden L. 2002. Notes on the path and wake of a gas bubble rising in pure water. *Int. J. Multiphase Flow* 28:1823–35
- Eiffel G. 1912. Sur la résistance des sphères dans l'air en mouvement. *C. R. Acad. Sci.* 155:1597–602
- Ellingsen K, Risso F. 2001. On the rise of an ellipsoidal bubble in water: oscillatory paths and liquid-induced velocity. *J. Fluid Mech.* 440:235–68
- Ern P, Fernandes PC, Risso F, Magnaudet J. 2007. Evolution of wake structure and wake-induced loads along the path of freely rising axisymmetric bodies. *Phys. Fluids* 19:113302
- Ern P, Risso F, Fernandes PC, Magnaudet J. 2009. A dynamical model for the buoyancy-driven zigzag motion of oblate bodies. *Phys. Rev. Lett.* 102:134505
- Fabre D, Assemat P, Magnaudet J. 2011. A quasi-static approach to the stability of the path of heavy bodies falling within a viscous fluid. *J. Fluids Struct.* 27:758–67
- Fabre D, Auguste F, Magnaudet J. 2008. Bifurcations and symmetry breaking in the wake of axisymmetric bodies. *Phys. Fluids* 20:051702
- Fernandes PC, Ern P, Risso F, Magnaudet J. 2005. On the zigzag dynamics of freely moving axisymmetric bodies. *Phys. Fluids* 17:098107
- Fernandes PC, Ern P, Risso F, Magnaudet J. 2008. Dynamics of axisymmetric bodies rising along a zigzag path. *J. Fluid Mech.* 606:209–23

- Fernandes PC, Risso F, Ern P, Magnaudet J. 2007. Oscillatory motion and wake instability of freely-rising axisymmetric bodies. *J. Fluid Mech.* 573:479–502
- Field SB, Klaus M, Moore MG, Nori F. 1997. Chaotic dynamics of falling disks. *Nature* 388:252–54
- Ford B, Loth E. 1998. Forces on ellipsoidal bubbles in a turbulent shear layer. *Phys. Fluids* 10:178–88
- Ghidersa B, Dusek J. 2000. Breaking of axisymmetry and onset of unsteadiness in the wake of the sphere. *J. Fluid Mech.* 423:33–69
- Gumowski K, Miedzik J, Goujon-Durand S, Jenffer P, Wesfreid JE. 2008. Wake behind a sphere in early transitional regimes. *Phys. Rev. E* 77:055308
- Horowitz M, Williamson CHK. 2006. Dynamics of a rising and falling cylinder. *J. Fluid Struct.* 22:837–43
- Horowitz M, Williamson CHK. 2010a. The effect of Reynolds number on the dynamics and wakes of freely rising and falling spheres. *J. Fluid Mech.* 651:251–94
- Horowitz M, Williamson CHK. 2010b. Vortex-induced vibration of a rising and falling cylinder. *J. Fluid Mech.* 662:352–83
- Howe MS. 1995. On the force and moment on a body in an incompressible fluid, with application to rigid bodies and bubbles at low and high Reynolds numbers. *Q. J. Mech. Appl. Math.* 48:401–26
- Jenny M, Dusek J. 2004. Efficient numerical method for the direct numerical simulation of the flow past a single light moving spherical body in transitional regimes. *J. Comput. Phys.* 194:215–32
- Jenny M, Dusek J, Bouchet G. 2004. Instabilities and transition of a sphere falling or ascending in a Newtonian fluid. *J. Fluid Mech.* 508:201–39
- Johnson TA, Patel VC. 1999. Flow past a sphere up to a Reynolds number of 300. *J. Fluid Mech.* 378:19–70
- Jones MA, Shelley MJ. 2005. Falling cards. *J. Fluid Mech.* 540:393–425
- Kim D, Choi H. 2003. Laminar flow past a hemisphere. *Phys. Fluids* 15:2457–60
- Kirchhoff G. 1869. Über die Bewegung eines Rotationskörpers in einer Flüssigkeit. *J. Reine Angew. Math.* 71:237–81
- Kozlov VV, Onischenko DA. 1982. Nonintegrability of Kirchhoff's equations. *Dokl. Math.* 26:495–98
- Kry PR, List R. 1974. Angular motions of freely falling spheroidal hailstone models. *Phys. Fluids* 17:1093–102
- Landau LD, Lifschitz EM. 1987. *Course of Theoretical Physics*, Vol. 6: *Fluid Mechanics*. Oxford: Butterworth-Heinemann. 2nd ed.
- Legendre D, Lauga E, Magnaudet J. 2009. Influence of slip on the dynamics of two-dimensional wakes. *J. Fluid Mech.* 633:437–47
- Lentink D, Dickson WB, van Leeuwen JL, Dickinson MH. 2009. Leading-edge vortices elevate lift of autorotating plant seeds. *Science* 324:1438–40
- Lugt HJ. 1980. Autorotation of an elliptic cylinder about an axis perpendicular to the flow. *J. Fluid Mech.* 99:817–40
- Lugt HJ. 1983. Autorotation. *Annu. Rev. Fluid Mech.* 15:123–47
- Lunde K, Perkins RJ. 1997. Observations on wakes behind spheroidal bubbles and particles. *Proc. ASME Fluids Eng. Div. Summer Meet.*, Pap. 97-3530
- Magarvey RH, Bishop RL. 1961a. Transition ranges for three-dimensional wakes. *Can. J. Phys.* 39:1418–22
- Magarvey RH, Bishop RL. 1961b. Wakes in liquid-liquid systems. *Phys. Fluids* 4:800–5
- Magarvey RH, MacLachy CS. 1965. Vortices in sphere wakes. *Can. J. Phys.* 43:1649–56
- Magnaudet J, Eames I. 2000. The motion of high-Reynolds-number bubbles in inhomogeneous flows. *Annu. Rev. Fluid Mech.* 32:659–708
- Magnaudet J, Mougin G. 2007. Wake instability of a fixed spheroidal bubble. *J. Fluid Mech.* 572:311–38
- Mahadevan L. 1996. Tumbling of a falling card. *C. R. Acad. Sci. Paris* 323:729–36
- Mahadevan L, Ryu W, Samuel A. 1999. Tumbling cards. *Phys. Fluids* 11:1–3
- Maxwell JC. 1853. On a particular case of the descent of a heavy body in a resisting medium. *Camb. Dublin Math. J.* 9:145–48
- Meliga P, Chomaz JM, Sipp D. 2009. Global mode interaction and pattern selection in the wake of a disk: a weakly nonlinear expansion. *J. Fluid Mech.* 63:159–89
- Mittal R. 1998. Planar symmetry in the unsteady wake of a sphere. *AIAA J.* 37:388–90
- Mittal R, Seshadri V, Udaykumar HS. 2004. Flutter, tumble, and vortex induced autorotation. *Theor. Comput. Fluid Dyn.* 17:165–70

- Mougin G, Magnaudet J. 2002a. The generalized Kirchhoff equations and their application to the interaction between a rigid body and an arbitrary time-dependent viscous flow. *Int. J. Multiphase Flow* 28:1837–51
- Mougin G, Magnaudet J. 2002b. Path instability of a rising bubble. *Phys. Rev. Lett.* 88:014502
- Mougin G, Magnaudet J. 2006. Wake-induced forces and torques on a zigzagging/spiralling bubble. *J. Fluid Mech.* 567:185–94
- Namkoong K, Yoo JY, Choi HG. 2008. Numerical analysis of two-dimensional motion of a freely falling circular cylinder in an infinite fluid. *J. Fluid Mech.* 604:33–53
- Natarajan R, Acrivos A. 1993. The instability of the steady flow past spheres and disks. *J. Fluid Mech.* 254:323–44
- Newton I. 1687. *Principia (Mathematical Principles of Natural Philosophy)*, Vol. 2. Transl. IB Cohen, A Whitman, 1999. Berkeley: Univ. Calif. Press
- Ormieres D, Provansal M. 1999. Transition to turbulence in the wake of a sphere. *Phys. Rev. Lett.* 83:80–83
- Pesavento U, Wang ZJ. 2004. Falling paper: Navier-Stokes solutions, model of fluid forces, and center of mass elevation. *Phys. Rev. Lett.* 93:144501
- Pier B. 2008. Local and global instabilities in the wake of a sphere. *J. Fluid Mech.* 603:39–61
- Prosperetti A. 2004. Bubbles. *Phys. Fluids* 16:1852–65
- Prosperetti A, Ohl CD, Tijink A, Mougin G, Magnaudet J. 2003. Leonardo's paradox: appendix to Ohl, Tijink & Prosperetti. 482:286–89
- Przadka A, Miedzik J, Goujon-Durand S, Wesfreid JE. 2008. The wake behind the sphere, analysis of vortices cores during the transition from steady to unsteady wake. *Arch. Mech.* 60:467–74
- Riboux G, Risso F, Legendre D. 2010. Experimental characterization of the agitation generated by bubbles rising at high Reynolds number. *J. Fluid Mech.* 643:509–39
- Shenoy AR, Kleinstreuer C. 2010. Influence of aspect ratio on the dynamics of a freely moving circular disk. *J. Fluid Mech.* 653:463–87
- Shew W, Poncet S, Pinton JF. 2006. Force measurements on rising bubbles. *J. Fluid Mech.* 569:51–60
- Smith EH. 1971. Autorotating wings: an experimental investigation. *J. Fluid Mech.* 50:513–34
- Stewart RE, List R. 1983. Gyration motion of disks during free fall. *Phys. Fluids* 26:920–27
- Stringham GE, Simons DB, Guy HP. 1969. The behavior of large particles falling in quiescent liquids. *US Geol. Surv. Prof. Pap.* 562-C, US Geol. Surv., Reston, VA
- Tanabe Y, Kaneko K. 1994. Behavior of a falling paper. *Phys. Rev. Lett.* 73:1372–75
- Thompson MC, Leweke T, Provansal M. 2001. Kinematics and dynamics of sphere wake transition. *J. Fluids Struct.* 15:575–85
- Tomboulides AG, Orszag SA. 2000. Numerical investigation of transitional and weak turbulent flow past a sphere. *J. Fluid Mech.* 416:45–73
- Veldhuis CHJ, Biesheuvel A. 2007. An experimental study of the regimes of motion of spheres falling or ascending freely in a Newtonian fluid. *Int. J. Multiphase Flow* 33:1074–87
- Veldhuis CHJ, Biesheuvel A, Lohse D. 2009. Freely rising light solid spheres. *Int. J. Multiphase Flow* 35:312–22
- Viets H, Lee DA. 1971. Motion of freely falling spheres at moderate Reynolds numbers. *AIAA J.* 9:2038–42
- Wang ZJ. 2005. Dissecting insect flight. *Annu. Rev. Fluid Mech.* 37:183–210
- Williamson CHK. 1996. Vortex dynamics in the cylinder wake. *Annu. Rev. Fluid Mech.* 28:477–539
- Williamson CHK, Govardhan R. 2004. Vortex-induced vibrations. *Annu. Rev. Fluid Mech.* 36:413–55
- Willmarth WW, Hawk NE, Harvey RL. 1964. Steady and unsteady motions and wakes of freely falling disks. *Phys. Fluids* 7:197–208
- Yang B, Prosperetti A. 2007. Linear stability of the flow past a spheroidal bubble. *J. Fluid Mech.* 582:53–78
- Zenit R, Magnaudet J. 2008. Path instability of spheroidal rising bubbles: a shape-controlled process. *Phys. Fluids* 20:061702
- Zenit R, Magnaudet J. 2009. Measurements of the streamwise vorticity in the wake of an oscillating bubble. *Int. J. Multiphase Flow* 35:195–203
- Zhong H, Chen S, Lee C. 2011. Experimental study of freely falling thin disks: transition from planar zigzag to spiral. *Phys. Fluids* 23:011702



Contents

Aeroacoustics of Musical Instruments <i>Benoit Fabre, Joël Gilbert, Avraham Hirschberg, and Xavier Pelorson</i>	1
Cascades in Wall-Bounded Turbulence <i>Javier Jiménez</i>	27
Large-Eddy-Simulation Tools for Multiphase Flows <i>Rodney O. Fox</i>	47
Hydrodynamic Techniques to Enhance Membrane Filtration <i>Michel Y. Jaffrin</i>	77
Wake-Induced Oscillatory Paths of Bodies Freely Rising or Falling in Fluids <i>Patricia Ern, Frédéric Risso, David Fabre, and Jacques Magnaudet</i>	97
Flow and Transport in Regions with Aquatic Vegetation <i>Heidi M. Nepf</i>	123
Electrorheological Fluids: Mechanisms, Dynamics, and Microfluidics Applications <i>Ping Sheng and Weijia Wen</i>	143
The Gyrokinetic Description of Microturbulence in Magnetized Plasmas <i>John A. Krommes</i>	175
The Significance of Simple Invariant Solutions in Turbulent Flows <i>Genta Kawahara, Markus Uhlmann, and Lennaert van Veen</i>	203
Modern Challenges Facing Turbomachinery Aeroacoustics <i>Nigel Peake and Anthony B. Parry</i>	227
Liquid Rope Coiling <i>Neil M. Ribe, Mehdi Habibi, and Daniel Bonn</i>	249
Dynamics of the Tear Film <i>Richard J. Braun</i>	267
Physics and Computation of Aero-Optics <i>Meng Wang, Ali Mani, and Stanislav Gordeyev</i>	299

Smoothed Particle Hydrodynamics and Its Diverse Applications <i>J. J. Monaghan</i>	323
Fluid Mechanics of the Eye <i>Jennifer H. Siggers and C. Ross Ethier</i>	347
Fluid Mechanics of Planktonic Microorganisms <i>Jeffrey S. Guasto, Roberto Rusconi, and Roman Stocker</i>	373
Nanoscale Electrokinetics and Microvortices: How Microhydrodynamics Affects Nanofluidic Ion Flux <i>Hsueh-Chia Chang, Gilad Yossifon, and Evgeny A. Demekhin</i>	401
Two-Dimensional Turbulence <i>Guido Boffetta and Robert E. Ecke</i>	427
“Vegetable Dynamics”: The Role of Water in Plant Movements <i>Jacques Dumais and Yoël Forterre</i>	453
The Wind in the Willows: Flows in Forest Canopies in Complex Terrain <i>Stephen E. Belcher, Ian N. Harman, and John J. Finnigan</i>	479
Multidisciplinary Optimization with Applications to Sonic-Boom Minimization <i>Juan J. Alonso and Michael R. Colonno</i>	505
Direct Numerical Simulation on the Receptivity, Instability, and Transition of Hypersonic Boundary Layers <i>Xiaolin Zhong and Xiaowen Wang</i>	527
Air-Entrainment Mechanisms in Plunging Jets and Breaking Waves <i>Kenneth T. Kiger and James H. Duncan</i>	563

Indexes

Cumulative Index of Contributing Authors, Volumes 1–44	597
Cumulative Index of Chapter Titles, Volumes 1–44	606

Errata

An online log of corrections to *Annual Review of Fluid Mechanics* articles may be found at <http://fluid.annualreviews.org/errata.shtml>